ARTICLE IN PRESS

Communications Earth & Environment https://doi.org/10.1038/s43247-026-03310-8

Article in Press

Distinct glacial-interglacial amplitudes of Asian monsoon water isotopes during the last deglaciation

Received: 13 September 2025

Accepted: 9 February 2026

Xiaoqing Wang, Weiyi Sun, Jian Liu, Liang Ning, Yuntao Bao, Kan Zhao, Jiazhi He, Yanan Ma, Kefan Chen, Qin Wen & Yongjin Wang

Cite this article as: Wang, X., Sun, W., Liu, J. *et al.* Distinct glacial-interglacial amplitudes of Asian monsoon water isotopes during the last deglaciation. *Commun Earth Environ* (2026). https://doi.org/10.1038/s43247-026-03310-8

We are providing an unedited version of this manuscript to give early access to its findings. Before final publication, the manuscript will undergo further editing. Please note there may be errors present which affect the content, and all legal disclaimers apply.

If this paper is publishing under a Transparent Peer Review model then Peer Review reports will publish with the final article.

ARTICLE IN PRESS

© The Author(s) 2026. **Open Access** This article is licensed under a Creative Commons Attribution-NonCommercial-NoDerivatives 4.0 International License, which permits any non-commercial use, sharing, distribution and reproduction in any medium or format, as long as you give appropriate credit to the original author(s) and the source, provide a link to the Creative Commons licence, and indicate if you modified the licensed material. You do not have permission under this licence to share adapted material derived from this article or parts of it. The images or other third party material in this article are included in the article's Creative Commons licence, unless indicated otherwise in a credit line to the material. If material is not included in the article's Creative Commons licence and your intended use is not permitted by statutory regulation or exceeds the permitted use, you will need to obtain permission directly from the copyright holder. To view a copy of this licence, visit http://creativecommons.org/licenses/by-nc-nd/4.0/.

Distinct glacial-interglacial amplitudes of Asian monsoon water isotopes during the last deglaciation

Xiaoqing Wang[1,2], Weiyi Sun[1,2*], Jian Liu[1,2], Liang Ning[1,2], Yuntao Bao[3,4], Kan Zhao[1,2], Jiazhi He[1,2], Yanan Ma[1,2], Kefan Chen[1,2], Qin Wen[1,2], and Yongjin Wang[1,2]

[1] State Key Laboratory of Climate System Prediction and Risk Management, Key Laboratory for Virtual Geographic Environment of Ministry of Education, Jiangsu Center for Collaborative Innovation in Geographical Information Resource Development and Application, Nanjing Normal University, Nanjing, China

[2] School of Geography, Nanjing Normal University, Nanjing, China

[3] Nanjing-Helsinki Institute in Atmospheric and Earth System Sciences, Nanjing University, Nanjing, China

[4] Department of Geography, The Ohio State University, Columbus, Ohio, USA

*Corresponding authors: Weiyi Sun, weiyisun@njnu.edu.cn

Abstract

Understanding Asian summer monsoon changes during the last deglaciation through the oxygen isotope offers insights into future hydroclimate. However, the cause of limited glacial-interglacial shifts in oxygen isotope over eastern China remains unknown. Here, combining oxygen isotope records with isotope-enabled climate simulations, we identify a pronounced east-west contrast in glacial-interglacial oxygen isotope amplitudes between South Asia (larger changes) and eastern China (muted signal), despite comparable precipitation changes. This contrast is driven primarily by ice-sheet forcing, with opposing effects from orbital and greenhouse-gas further damping the isotope response in eastern China. Water-tagging experiments reveal that the weaker eastern China signal reflects competing processes: depletion primarily driven by increased Pacific-sourced moisture from a strengthened northwestward-shifted Western Pacific Subtropical High, alongside enrichment resulting from reduced rainout and enhanced local recycling over the marginal seas. These findings mechanistically reconcile puzzling differences between water isotope and other hydrological proxies across monsoon region on glacial-interglacial variability.

Introduction

The Asian Summer Monsoon (ASM) is a key component of the climate system, with its evolution profoundly influencing regional climates and feeding back into global climate change. Given ASM's complex dynamics and the uncertainty surrounding its response to ongoing warming[1–3], examining its behavior during past glacial–interglacial transitions offer a valuable analogue for understanding future monsoon dynamics.

There has been a long debate regarding the orbital-scale dynamics of the ASM, manifested in substantial differences in the periodic patterns revealed by different climate proxies[4–7]. Magnetic susceptibility records from the Chinese Loess Plateau exhibit a dominant ~100 ka cycle, aligning with global ice volume changes and showing a strong glacial-interglacial variability[8–10]. In contrast, cave speleothem oxygen isotopes ($\delta^{18}O_c$) in eastern China, a widely used proxy of ASM variability, display a prominent ~23 ka precession cycle and lack a glacial-interglacial signal, controlled by the Northern Hemisphere summer insolation[5,11]. The stark contrast in dominant periodicities between loess and $\delta^{18}O_c$ points to a fundamental disagreement on the orbital-scale forcing mechanisms of the ASM. This unresolved discrepancy suggests that $\delta^{18}O_c$ records in eastern China seem to be insensitive to ice sheet forcing and their hydroclimatic representation remains unclear.

Recently, several $\delta^{18}O_c$ records from South and Southeast Asia have shown a clear glacial-interglacial variation, in contrast to the muted signals observed in eastern China. For instance, the Xiaobailong Cave record from southwestern China exhibits a prominent ~100 ka cycle, influenced by the Indian summer monsoon (ISM)[12]. Model-based quantitative estimates indicate that the glacial-interglacial differences in precipitation oxygen isotope ($\delta^{18}O_p$) are substantial in South Asia (~2.0–4.0‰), roughly double those in eastern China (~1.0–2.0‰)[12]. Similarly, records from sites near the eastern Bay of Bengal display a clear glacial-interglacial $\delta^{18}O_c$ shift of ~3.7‰ since the Last Glacial Maximum (LGM), which lies along the ISM trajectory[13]. These findings suggest that in ISM-dominated regions, $\delta^{18}O_c$ records may capture glacial-interglacial changes. By contrast, $\delta^{18}O_c$ changes over eastern China are more complex, potentially reflecting changes in moisture transport pathways and sources[13], exposure of the "land bridge" in the Maritime continents[12], or shifts in the summer-to-annual precipitation ratio[14]. The relative importance of these mechanisms remains debated.

Isotope-enabled climate modeling offers a powerful tool for investigating glacial-interglacial variations in $\delta^{18}O_p$ and their hydroclimatic implications[15–17]. Transient simulations of the last deglaciation demonstrate that millennial-scale variability in ASM $\delta^{18}O_p$ responds to both meltwater and insolation forcings, with contributions from changes in upstream moisture sources from the Indian and Pacific Oceans[18–20]. However, these studies mainly consider $\delta^{18}O_p$ variability associated with millennial-scale events, and do not systematically address long-term glacial-interglacial trends. More recent simulations spanning the past 300 ka suggest that $\delta^{18}O_p$ in the East Asian Monsoon region is influenced not only by precessional forcing but also by ice sheet forcing[14,21]. For example, Liu et al.[21] proposed that the April–May $\delta^{18}O_p$ signal is driven by ice-sheet forcing, whereas the annual mean $\delta^{18}O_p$ is dominated by its August–September variation in response to orbital forcing. Additionally, Zhang et al.[14] demonstrated that a lower summer-to-annual precipitation ratio in eastern China can offset the impact of the low summer $\delta^{18}O_p$ values, thereby weakening the interglacial peak signal. Together, they highlight that ASM $\delta^{18}O_p$ variability across millennial and orbital timescales is driven by meltwater, orbital, and ice-sheet forcings, mediated by distinct processes including the local amount effect[14,19,21], enroute rainout[18,20], and moisture source changes[19,22]. Despite these advances, the $\delta^{18}O_p$ characteristics and mechanisms of glacial-interglacial changes in South Asia and East Asia, particularly the processes underlying the muted $\delta^{18}O_p$ response in eastern China, remain unresolved.

$\delta^{18}O_c$ and other hydrological proxy data are abundant during the last deglaciation (20–11 ka), but studies explicitly addressing the amplitude of $\delta^{18}O_p$ changes in the ASM region remain limited. To address this gap, we focus on three questions: (1) How did the amplitudes of glacial–interglacial $\delta^{18}O_p$ changes evolve across the Asian monsoon region during the last deglaciation? (2) What processes shaped the spatial pattern of these isotope changes? (3) How did different external forcings contribute to regional differences in isotopic amplitude? We address these questions by combining the hydroclimatic proxy records with state-of-the-art isotope-enabled transient climate simulations covering the last deglaciation (iTRACE)[18]. Our analysis compares two representative climatic states, the LGM (20–19.5 ka) and the early Holocene (11.5–11 ka), to identify the primary characteristic response to the glacial-interglacial transition. We then conduct water-tagging experiments to trace and decompose the source-transport-sink processes of $\delta^{18}O_p$ in South Asia (10–25°N, 70–105°E) and eastern China (22.5–40°N, 105–120°E), and integrate these with sensitivity experiments to assess the influence of external forcings on monsoon precipitation and $\delta^{18}O_p$.

Result

Distinct glacial-interglacial $\delta^{18}O$ amplitudes over South Asia and eastern China

To investigate glacial-interglacial $\delta^{18}O_c$ changes during the last deglaciation, we compare temporal variations in both reconstructed and simulated $\delta^{18}O_c$ over South Asia and eastern China (Fig. 1; Supplementary Fig. 1). The most prominent feature in the proxy data is the significantly more depleted $\delta^{18}O_c$ values over South Asia, with an ensemble mean shift of approximately −1.5‰ between the early Holocene and LGM. This is evident in records from Mawmluh Cave[23] and eastern coastal Bay of Bengal caves[13], show very large depletions of about −2.4‰ and −2.6‰, respectively. Records form southeastern Yunnan caves[13] also exhibits a change of −1.5‰. Although the Xiaobailong Cave record[12] is slightly enriched during the 20–11 ka interval, the glacial–interglacial amplitude remains pronounced over longer timescales (Supplementary Fig. 1). Excluding the Xiaobailong record, which might be influenced by dating uncertainty around the Younger Dryas[12], the mean $\delta^{18}O_c$ shift in South Asia reaches −2.2‰ (Supplementary Fig. 1c). In contrast, eastern China shows smaller changes, averaging around −1.1‰ (Fig. 1b–c; Supplementary Fig. 1). For example, the high-resolution $\delta^{18}O_c$ record in Hulu Cave[24,25] exhibits a change of less than −1‰ and more recent long-term records from Haozhu Cave[26], Luoshui Cave[27] and Furong Cave[28] in southwestern China show an amplitude change only approximately −1.2‰. This amplitude contrast is captured by iTRACE climate simulation, which shows greater $\delta^{18}O_c$ changes in South Asia (−1.5‰; Fig. 1b) than in eastern China (−0.4‰; Fig. 1c), despite a known systematic positive bias[18] in simulated $\delta^{18}O_p$ over East Asia. These differences in temporal amplitude confirm a robust east-west contrast in isotopic amplitude response across the Asian monsoon region during the glacial-interglacial transition.

Spatial pattern of glacial-interglacial $\delta^{18}O_p$ changes over the ASM region between the early Holocene and LGM reveals a strong east-west sign contrast (Fig. 1a). Western Asia—including South Asia and the Tibetan Plateau, west of approximately 105°E—exhibits widespread $\delta^{18}O_p$ depletion, while eastern China displays a much weaker response (Fig. 1a). A transitional zone across central-eastern and southeastern China displays relatively stable $\delta^{18}O_p$ values, consistent with the small amplitude changes recorded in Furong, Luoshui and Haozhu caves. Notably, although the simulation displays a localized positive bias along the East Asian coast (near 120°E), which may reflect region-specific biases in modeled coastal moisture transport or convection[18], the simulated pattern successfully captures the dominant east-west spatial contrast. The robust consistency between simulated and reconstructed spatial patterns confirms a robust east-west difference in isotopic changes across the Asian monsoon region during the glacial-interglacial transition.

Glacial-interglacial changes in Asian monsoon precipitation and circulation

To assess whether the $\delta^{18}O_p$ amplitude differences reflect actual hydrological changes, we examine glacial-interglacial precipitation variations. In South Asia, terrestrial precipitation increased substantially from the LGM to the early Holocene, as evidenced by pollen-based reconstructions from Tengchongqinghai and Caohai Lakes[29] (increase ~300 mm year^{-1}) and sediment reflectance from the northeastern Arabian Sea[30] (Supplementary Fig. 2b). Similarly, in North China, enhanced precipitation is indicated by increased loess magnetic susceptibility from the Gulang and Jingyuan sections[31] and pollen reconstructions from Gonghai[32] (Supplementary Fig. 2c). In contrast, southern China experienced a precipitation decline, shown by both pollen records from Gutian[33] (decrease ~200 mm year^{-1}) and speleothem trace-element data from Haozhu Cave[26] (Supplementary Fig. 2d). Our simulations reproduce this pattern, capturing pronounced wetting over South Asian continent and North China but a distinct response in South China, which establishes a clear north-south precipitation contrast across eastern China (Fig. 2b; Supplementary Fig. 2). A fundamental spatial disconnect thus exists between the coherent $\delta^{18}O_p$ depletion and the regional precipitation changes, indicating that local rainfall cannot solely account for the isotopic signal across ASM region.

To explore the reason behind this precipitation pattern, we examined monsoon circulation changes. Such a continental-scale north-south precipitation footprint during periods of intensified monsoon has been linked in modeling studies to a coherent large-scale adjustment of the Asian monsoon system[22]. In the iTRACE simulation, relative to the climatological mean, the East Asian Summer monsoon (EASM) intensified, accompanied by a northwestward displacement of the western Pacific Subtropical High (WPSH, Fig. 2a−c)[34]. The EASM circulation index—defined as the 850-hPa mean meridional wind (V850) at 20°–45°N, 110°–130°E[35]—indicates a strengthening of ~1.4 m s^{-1} from the LGM to the early Holocene. Enhanced southerly winds over southeastern China promoted ascending motion in northern China but descending motion in the south, causing the north-south dipole pattern of precipitation (Fig. 2b and d). This circulation change provides a dynamical explanation for the heterogenous rainfall response that decouples from the homogeneous $\delta^{18}O_c$ signal. Meanwhile, the strengthened WPSH and North Pacific anticyclonic anomalies likely enhanced the transport of heavier, locally sourced $\delta^{18}O_p$ from the western Pacific into eastern China.

Over South Asia, easterly anomalies over the Bay of Bengal increased moisture transport from the Indo-Pacific warm pool, thereby intensifying precipitation over Indian subcontinent. The Indian summer monsoon circulation index—defined as the meridional shear of 850-hPa zonal winds (U850) at 10°–20°N, 40°–80°E and 25°–32.5°N, 75°–90°E[36]—indicates a strengthening of ~0.5 m s^{-1} from the LGM to the early Holocene. However, cross-equatorial flow over the western Indian Ocean weakened markedly, challenging the prevailing view that a stronger ISM primarily drove greater moisture transport from the equatorial and southern Indian Ocean to the Asian monsoon region[16]. This weakening would have reduced the transport of long-distance moisture from southern Indian Ocean sources to eastern China.

Processes influencing the relatively muted $\delta^{18}O_p$ response in eastern China

To quantitatively assess the contributions of different moisture sources, we conducted two snapshot water-tagging experiments for the LGM and Early Holocene. The climatological $\delta^{18}O_p$

over the Asian monsoon region during the LGM primarily originated from the Indian Ocean, contributing approximately 62% to South Asia and 33% to eastern China (Supplementary Fig. 3). However, the Pacific Ocean accounted for only ~12% and ~25% of the $\delta^{18}O_p$ in these regions, respectively, which is consistent with findings by He et al.[18]. From LGM to 11 ka, the changes in $\delta^{18}O_p$ in eastern China can be explained by a reduction in Indian Ocean moisture contribution (to ~23% at 11 ka) and a concurrent increase in Pacific-sourced moisture (to ~40% at 11 ka, Supplementary Fig. 3r), particularly from the subtropical North Pacific (SNP) and the west equatorial Pacific (WEP; Supplementary Fig. 3l and n). The patterns of the precipitation moisture (^{16}O) source (Supplementary Fig. 4) closely mirror those of $\delta^{18}O_p$ origin, further supporting the enhanced role of Pacific moisture in shaping $\delta^{18}O_p$ over eastern China.

The east-west amplitude contrast in $\delta^{18}O_p$ changes between 11 ka and the LGM can be further decomposed into: the changes associated with the relative moisture contribution from different source regions ($\Delta\frac{P_i}{P}\times\delta^{18}O_{p,i}$) and the intrinsic $\delta^{18}O_p$ composition in the sink region ($\Delta\delta^{18}O_{p,i}\times\frac{P_i}{P}$) (Equation 4a). In South Asia, $\delta^{18}O_p$ depletion is almost entirely attributed to changes in the moisture source contributions (−1.20‰ out of −1.15‰; Fig. 3a). In contrast, eastern China experiences a compensating effect between the moisture source contribution changes and the intrinsic $\delta^{18}O_p$ composition changes (Fig. 3a–b). The source contribution change accounts for a $\delta^{18}O_p$ decrease of −0.97‰, resulting in a much smaller net $\delta^{18}O_p$ change. The Pacific Ocean is the dominant driver of the intrinsic composition enrichment in eastern China, contributing +0.55‰ out of the total +0.85‰ (Fig. 3d), partially offsetting the depletion caused by precipitation-weighted changes. Further decomposition of this intrinsic $\delta^{18}O_p$ component ($\Delta\delta^{18}O_{p,i}\times\frac{P_i}{P}$) (Equation 4b) reveals that this enrichment in eastern China stems from both enroute or upstream rainout (+0.64‰) and local condensation processes (+0.40‰; Supplementary Fig. 5a–b).

Collectively, the relatively muted $\delta^{18}O_p$ over eastern China arises from the combined effects of moisture source contribution changes and intrinsic $\delta^{18}O_p$ component changes. On one hand, $\delta^{18}O_p$ depletion in eastern China documents the change of moisture source location associated with atmospheric circulation processes: the strengthening and northwestward of WPSH strengthened easterly anomalies over the western North Pacific (Fig. 2c), leading to an increased relative contribution of the Pacific moisture (due $\Delta\frac{P_i}{P}\times\delta^{18}O_{p,i} < 0$ and $\delta^{18}O_{p,i} < 0$, then $\Delta\frac{P_i}{P} > 0$, Fig. 3c). Simultaneously, anomalous warming over the Maritime Continent (MC) enhanced convective heating, which excited northwestward-propagating Rossby waves along the monsoon flow. These waves established an anomalous cyclonic circulation over the northwestern Arabian Sea (Fig. 2b), weakening the Somali Jet and thereby suppressing moisture transport from the southern Indian Ocean (due $\Delta \frac{P_i}{P} \times \delta^{18}O_{p,i} > 0$ and $\delta^{18}O_{p,i} < 0$, then $\Delta \frac{P_i}{P} < 0$, Fig. 3e). On the other hand, and more notably, reduced enroute depletion together with a net enrichment from local condensation changes led to an enrichment in $\delta^{18}O_p$ in eastern China (Supplementary Fig. 5a–b). The decrease in enroute depletion primarily arose from two mechanisms: firstly, the shortened moisture transport path from the Pacific weakened Rayleigh fractionation effects[13] during transmission (Supplementary Fig. 5c); and secondly, the weakened cross-equatorial flow hindered the downstream transport of Indian Ocean moisture (Supplementary Fig. 5e). Changes in local condensation, notably enhanced re-evaporation of sub-cloud rainfall under drier conditions, contributed significantly to $\delta^{18}O_p$ enrichment, which is supported by enhanced evaporation over East Asian land and marginal seas (Supplementary Fig. 6a). Therefore, in eastern China, enrichment from shortened moisture transport and enhanced local evaporation partially compensates for the depletion caused by the increasing contribution of Pacific-sourced moisture, leading to a relatively muted net $\delta^{18}O_p$ response.

Influence of different external forcings on the $\delta^{18}O_p$ pattern

To identify the drivers of the $\delta^{18}O_p$ response, we quantified the effects of individual forcings using the iTRACE sensitivity experiments (Fig. 4). ICE forcing emerges as the dominant control on the ASM east-west $\delta^{18}O_p$ contrast, explaining ~54% of the difference between South Asia and eastern China (0.83‰ out of 1.54‰; Fig. 4a–b, e). The close match between $\delta^{18}O_p$ pattern over the ASM region from ICE forcing and those from the all-forcing experiment ($r = 0.81$, $p < 0.01$) further underscores its importance. In comparison, orbital insolation (ORB) forcing produces a broadly uniform $\delta^{18}O_p$ depletion across the monsoon region, while greenhouse gases (GHG) forcing induces enrichment (Fig. 4c–d). Together, ORB and GHG forcing account for a secondary contribution (~45%; 0.24‰ + 0.46‰) to the east-west contrast. These two forcings modulate the $\delta^{18}O_p$ amplitudes in opposite directions over eastern China.

In South Asia, $\delta^{18}O_p$ depletion was influenced by the combined effects of ICE and ORB forcings (Fig. 4b–c). From the LGM to the early Holocene, ice sheet retreat caused global warming that intensified continental warming relative to the North Pacific. Ice sheet melting raised sea level, inundating more land over the MC and promoting regional warming[37]. The resulting increase in MC convection and precipitation generated northwestward-propagating Rossby waves, reinforcing cyclonic circulation over the northern Indian Ocean (Fig. 5 a–b). This circulation changes boosted Indian precipitation and further drove greater $\delta^{18}O_p$ depletion there (Supplementary Fig. 3i–n). ORB forcing reinforced this pattern, as enhanced Northern Hemisphere summer insolation strengthened the ISM and increased precipitation over India, consistent with earlier studies[22].

From the LGM to the early Holocene, the retreat of the North America-European ice sheets induced a midlatitude upper-level zonal wave train that propagated to the North Pacific, forming a barotropic structure (Supplementary Fig. 7). Combined with an enhanced land-sea thermal contrast between Asia and the North Pacific, this strengthened the anomalous North Pacific High, leading to a westward extension of the WPSH and the formation of a strong northwestern Pacific anticyclone (Fig. 5). This circulation brought more $\delta^{18}O_p$-depleted Pacific-sourced moisture into eastern China, contributing to depletion in $\delta^{18}O_p$ (Fig. 3c). However, the relatively shorter moisture transport pathway from the western Pacific—compared to that of the Indian Ocean—weakened the Rayleigh distillation effect during vapor transport from source to sink regions (Fig. 3d). A reduced moisture supply from the Indian Ocean further diminished the tendency for $\delta^{18}O_p$ depletion (Fig. 3f). These processes collectively promoted $\delta^{18}O_p$ enrichment tendency in eastern China. In addition, sea-level rise from ice sheet melting inundated parts of the eastern China coastal plain, enhancing evaporation from local seawater (Supplementary Fig. 6) and further enriching $\delta^{18}O_p$. A similar anomalous circulation pattern appears in both the all-forcing and ICE forcing experiments from TRACE-21ka (Supplementary Fig. 8). Under GHG-induced global warming, intensified oceanic and terrestrial evaporation (Supplementary Fig. 6d) increased atmospheric moisture content. Eastern China and adjacent coastal areas experienced stronger local evaporation and moisture recycling, which contributed to further $\delta^{18}O_p$ enrichment (Supplementary Fig. 5d and h).

Conclusion and Discussion

In summary, this study combined speleothem records and isotope-enabled transient simulations to investigate the Asian monsoon $\delta^{18}O_p$ changes during the last deglaciation. We demonstrate a pronounced east-west contrast in glacial-interglacial $\delta^{18}O_p$ amplitude, with large $\delta^{18}O_p$ shifts in South Asia but relatively muted changes in eastern China, which differs from the north-south precipitation pattern. Attribution experiments identify ICE forcing as the primary driver, which explains 54% of the east-west contrast. ORB and GHG forcings make a secondary contribution whose opposing effects further weaken the $\delta^{18}O_p$ response in eastern China. Tagging experiments further revealed that this $\delta^{18}O_p$ contrast stemmed from competing processes in eastern China (Fig. 6): a shift in moisture source from the Indian Ocean to the subtropical North Pacific and western equatorial Pacific depleted $\delta^{18}O_p$ by −0.97‰, while weakened enroute depletion, combined with intensified local evaporation over marginal seas, enriched $\delta^{18}O_p$ by +1.04‰. Mechanistically, ice retreat raised sea level, increasing inundation and convection over the MC, generating Rossby wave responses that strengthened cyclonic circulation over the northern Indian Ocean. This circulation changes enhanced Indian precipitation, amplifying $\delta^{18}O_p$ depletion in South Asia. Eastern China experienced a greater influence of Pacific-sourced moisture linked to a stronger and more northwestward WPSH, while shorter transport paths and enhanced local recycling offset this depletion, producing a muted net isotope change.

While the simulations successfully reproduce the observed east-west contrast in $\delta^{18}O_p$ amplitude, the absolute simulated $\delta^{18}O_p$ values over eastern China show a systematic positive bias, with notable enrichment near ~120°E (Fig. 1a). This discrepancy likely stems from several factors inherent to current climate modeling: uncertainties in simulating East Asian monsoon circulation and its interaction with complex topography[18,38,39], potential biases in regional moisture source contributions and rainout processes[15,16,22], the scale mismatch between the model's coarse resolution and local cave environments[22,40], and the prescribed fixed pre-industrial land cover (which excludes vegetation feedbacks). Additionally, speleothem $\delta^{18}O_c$ integrates regional hydroclimatic signals rather than reflecting only local rainfall[11,16] complicating direct point-to-grid comparisons. Critically, this systematic bias does not invalidate the primary spatial pattern identified. Our central conclusion rests on the relative difference in $\delta^{18}O_p$ amplitude between regions, not on absolute values. The simulated contrast between a strongly depleted South Asia and a weakly responding eastern China also aligns robustly with reconstructed evidence across different timescales[12,41,42]. Hence, the east-west contrast of $\delta^{18}O_p$ is a robust feature of the model output. Future work with higher-resolution models, refined isotope-enabled schemes, and detailed moisture tracking will help reduce these biases and further elucidate regional hydrological processes.

Our study concentrates on the last deglaciation, due to limitations in simulation duration and computational resources. Although this time span is relatively short compared to full glacial–interglacial cycles, it captures a key transitional period with well-documented forcings and responses, providing a clear view of the processes controlling $\delta^{18}O_p$ amplitudes. We offer a mechanistic explanation for the weak ~100 ka signal in Chinese speleothem $\delta^{18}O_c$ records: the counteracting effects of increased Pacific-sourced moisture and enhanced local evaporation dampen the net isotopic variability between glacial and interglacial states. These processes are likely representative of broader glacial–interglacial dynamics, as supported by longer-term geological records and modeling studies. For instance, the $\delta^{18}O_c$ record shows larger changes in South Asia than in eastern China at 180 ka[13], reflecting the dominant role of ice sheet forcing in amplifying isotope distillation along the moisture transport pathways, which progressively counteracts the glacial-interglacial $\delta^{18}O_c$ signal over eastern China. Moreover, a 300 ka ORB + GHG + ICE transient simulation by Liu et al.[21] reveals that $\delta^{18}O_p$ in South Asia has a significant ~23 ka precession cycle and ~100 ka cycle, whereas $\delta^{18}O_p$ in East Asia is dominated only by the ~23 ka cycle. Therefore, the identified mechanisms are consistent with longer-term records and models, underscoring the generalizability of our conclusions across orbital timescales.

This work provides critical insights for reconciling divergent hydrological proxies in the Asian monsoon region on the orbital-scale. We demonstrate that the weaker glacial-interglacial $\delta^{18}O_p$ signal in eastern China does not indicate a weak hydroclimate response, but rather reflects compensatory processes in atmospheric moisture routing and local recycling, primarily orchestrated by ice-sheet forcing. In contrast, loess magnetic susceptibility from northern China, directly coupled to precipitation, preserve a strong ~100 ka period[8–10]. Thus, the apparent discrepancy between speleothem $\delta^{18}O_c$ (reflective of integrated circulation and water-source changes) and loess records (indicative of local rainfall) arises from their sensitivity to different aspects of the monsoon system. Reconciling these proxies thus requires the process-based perspective offered here, which moves beyond direct rainfall-$\delta^{18}O_p$ correlations to incorporate moisture origin, transport, and recycling. Furthermore, this notion—that hydrological responses are governed by competing processes rather than linear forcing—finds a clear analogy in future climate projections[43]. Specifically, our identified mechanism implies that under future greenhouse-gas-dominated warming, changes in moisture sources and land-atmosphere interactions are likely to persist and may even obscure the local precipitation signal in water-isotope records. Therefore, reliable projections of regional hydroclimate must account not only for precipitation changes but also for these non-local processes, which can fundamentally modulate the isotopic and hydrological expression of monsoon variability.

Materials and methods

Hydroclimatic proxy data

To evaluate the reliability of our model simulations, we compared climate simulations with speleothem $\delta^{18}O_c$ records from 8 caves across the Asian monsoon region, focusing on glacial–interglacial responses in South Asia and eastern China during the last deglaciation (Supplementary Table 1; Supplementary Fig. 1). Only records with robust geographic and chronological controls were included. South Asian records were restricted to caves explicitly within the ISM domain or whose $\delta^{18}O_c$ signals were definitively linked to ISM changes in source literature. These include southeastern Yunnan caves[13], eastern coastal Bay of Bengal caves[13], Mawmluh Cave[23], and Xiaobailong Cave in eastern Yunnan[12]. All records cover the entire last deglaciation interval with a mean temporal resolution finer than 78 years. East Asian records were drawn from datasets unequivocally attributed to the East Asian Monsoon, which includes Furong Cave[28], Luoshui Cave[27], Hulu Cave[24,25], and Haozhu Cave[26]. These records exhibit mean temporal resolutions finer than 35 years. To compare long-term trends between the proxy records and simulations, we calculated anomalies for each record by subtracting its mean value (Fig. 1b−c).

This study also collected multiple proxy reconstructions of precipitation changes during the last deglaciation. The South Asian datasets include total sediment reflectance and pollen-based reconstructions of annual mean precipitation (Supplementary Fig. 2). The sediment total reflectance from the northeastern Arabian Sea is used here as a proxy for the intensity of terrestrial precipitation associated with the ISM intensity[30]. Pollen records, statistically calibrated against modern climate data, reliably reflect past ISM precipitation, including those from the Tengchong-Qinghai volcanically dammed lake in Yunnan and the protected Caohai lake of Guizhou[29]. For northern China, the magnetic susceptibility of Chinese loess is widely regarded as a proxy for EASM precipitation, revealing a close link to global ice volume changes inferred from deep-sea oxygen isotopes[7]. We compiled original magnetic susceptibility from the Gulang and Jingyuan loess deposits on the Chinese Loess Plateau[31], which reflect precipitation changes in northern

China. Additionally, though limited by its temporal coverage (since 14.7 ka), the Gonghai pollen record[32] provides a high-quality dataset suitable for spatial comparisons of pollen-inferred precipitation changes over northern China. In southern China, the principal component of trace elements ratios (Mg/Ca, Sr/Ca, and Ba/Ca) from Haozhu Cave (HZZ PC1)[26] is used to reflect precipitation in South China. Furthermore, pollen from Gutian[33] in the Yuecheng Mountains, west of the Nanling Mountains, records the strong influence of the monsoon system and serves as another indicator of annual mean precipitation changes in South China. A summary of all precipitation proxies is shown in Supplementary Table 2.

Climate model simulations

We employed the isotope-enabled Transient Climate (iTRACE) simulations, which covers the period from the Last Glacial Maximum to the early Holocene[18]. The simulations were conducted using the isotope-enabled Community Earth System Model (iCESM) version 1.3, which explicitly simulates the transport and transformation of water isotopes across Earth system components[44,45].

All transient experiments were branched from a fully spun-up LGM simulation at 20 ka. This LGM state serves as the control (LGM Control) run for our analysis, and the climatic responses discussed hereafter are calculated as anomalies relative to this baseline. A series of sensitivity experiments were then performed: the simulation was driven by changes in ice sheet and ocean bathymetry (ICE)[18]. Land cover conditions between 20 ka and 11 ka were based on pre-industrial (PI) conditions, and the land–sea mask was updated according to ice-sheet evolution excluding vegetation-climate feedbacks. Orbital insolation forcing was then added (ICE + ORB)[46], followed by the inclusion of greenhouse gas concentrations (ICE + ORB + GHG)[47], and finally meltwater fluxes (ICE + ORB + GHG + MWF)[48], completing the all-forcing iTRACE simulation. To disentangle the role of each driver, we quantify the incremental effect of each added forcing factor under the assumption that forced responses are approximately linear: ice sheet and land-sea configuration changes (ICE – LGM Control), orbital forcing (ICE + ORB – ICE), greenhouse gases (ICE + ORB + GHG – ICE + ORB), and meltwater fluxes (ICE + ORB + GHG + MWF – ICE + ORB + GHG)[18]. In this study, the term "ICE forcing" (or "under/response to ICE forcing") refers specifically to this calculated response (ICE – LGM Control). By comparing two periods with minimal net meltwater forcing (20–19.5 ka vs. 11.5–11 ka), we isolate the long-term the impact of ICE, ORB, and GHG forcing factor (Fig. 4).

The iTRACE simulation exhibits a systematic bias in simulated $\delta^{18}O_p$, particularly over the East Asian monsoon region[18]. This bias might stem from an overestimation of deep convection in the atmospheric model component[49], which enhances rainout and leads to an excessive depletion of $\delta^{18}O_p$[44]. Consequently, simulated $\delta^{18}O_p$ amplitudes during the deglaciation are generally lower than speleothem records. In this context, the simulated difference in $\delta^{18}O_p$ between the two periods examined here may appear more positive than the corresponding changes in speleothem $\delta^{18}O$. However, this bias can be largely uniform in space and persistent through time[18]. We therefore focus on relative changes rather than absolute values and the identified patterns are considered robust.

For cross-validation, we also compared iTRACE results with TRACE-21ka simulations[48], which include an all-forcing run and four corresponding single-forcing experiments (i.e., ICE, ORB, GHG, and MWF). This comparison ensures the robustness of the simulated circulation patterns under different external forcings during the last deglaciation.

Simulated cave $\delta^{18}O$

To enable direct comparison between modeled $\delta^{18}O_p$ and speleothem $\delta^{18}O_c$, the simulation results require systematic preprocessing. First, precipitation-weighted $\delta^{18}O$ ($\delta^{18}O_p$) values are calculated from the raw model data using established methods (Equation 1)[50].

$$\delta^{18}O_P = \sum_{m=1}^{12} \frac{P_m}{P} \times \delta^{18}O_m \tag{1}$$

where m denotes the calendar month, P_m is precipitation from month m, $\delta^{18}O_m$ is the $\delta^{18}O$ from month m, and P is annual total precipitation.

Because speleothem calcite $\delta^{18}O_c$ differs from $\delta^{18}O_p$ due to temperature-dependent isotope fractionation during calcite precipitation, further transformations are needed (Equation 2a−b). Following the approach of Coplen et al.[50], the $\delta^{18}O_{p\text{-SMOW}}$ is converted into the water $\delta^{18}O$ scale ($\delta^{18}O_{p\text{–PDB}}$) as:

$$\delta^{18}O_{p-PDB} = 0.97002 \times \delta^{18}O_{P-SMOW} - 29.98 \tag{2a}$$

This is then transformed into $\delta^{18}O_c$ using the temperature-dependent equilibrium fractionation equation for inorganic carbonates[51]. This procedure, applied in previous studies[22,52], ensures that model-derived isotope values are directly comparable with speleothem records from cave archives. Shown as:

$$\delta^{18}O_c = \delta^{18}O_{P-PDB} + 2.70 \times 10^6/T^2 - 3.29 \tag{2b}$$

Here T is the model surface air temperature (unit: K), which represents the model annual mean temperature on the cave site.

Specially, $\delta^{18}O_c$ variability within the Asian monsoon domain is contributed primarily by fluctuations in $\delta^{18}O_p$, a mechanistic linkage consistent with the findings of He et al.[18]. Moreover, the direct influence of temperature on $\delta^{18}O_p$ is both statistically weak and quantitatively minor relative to the observed isotopic shifts. Consequently, beyond model–proxy comparisons (Fig. 1b–c), our analysis focuses on $\delta^{18}O_p$ as the key diagnostic variable for investigating large-scale climatic mechanisms. This choice minimizes the confounding influence of temperature-dependent processes during speleothem formation, ensuring that our interpretation remains centered on hydrological dynamics.

Tagging experiments

Water-tagging is a method for tracing water vapor sources based on isotope labeling techniques. It quantifies the isotopic composition of the source regions, enabling the tracing of water vapor transport pathways and phase-change processes in the atmosphere[53]. Unlike the traditional trajectory models such as HYSPLIT[54], water-tagging not only accounts for transport routes but also simulates the influence of physical processes on isotopic characteristics, providing a more comprehensive framework to analyze contributions of different sources to $\delta^{18}O_p$.

In this study, two water tagging experiments were conducted for the LGM (20 to 19.5 ka) and the early Holocene (11.5 to 11.0 ka). The experiments utilized the atmospheric component iCAM5.3, forced by boundary conditions derived from 500-year mean climatological states of two periods. These conditions included: sea surface temperature, sea ice, sea surface $\delta^{18}O$ and δD extracted from iTRACE, along with continental ice sheets, orbital parameters, and GHG concentrations. Each experiment was integrated for 20 years, with the last 10 years used for analysis.

For the Asian monsoon, the $\delta^{18}O_p$ and precipitation responses to glacial-interglacial changes in the tagging experiments (Supplementary Fig. 3i, 4i) resemble those in iTRACE simulations (Fig.

1a and Supplementary Fig. 2a). The global source regions were divided into 25 subregions: 13 oceanic and 12 terrestrial regions. At each grid point, precipitation (P) and $\delta^{18}O_p$ are computed as the sum of contributions from all source regions[18]:

$$P = \sum_{i=1}^{25} Pi \tag{3a}$$

$$\delta^{18}O_p = \sum_{i=1}^{25} \delta^{18}O_{p,sink,i}\left(\frac{P_i}{P}\right) \tag{3b}$$

Where P_i and $\delta^{18}O_i$ represent the precipitation and $\delta^{18}O_p$ at sink region originating from the tagged region i. The P_i /P denotes the relative precipitation contribution from the tagged source region i.

Decomposing $\delta^{18}O_p$ change

Changes in $\delta^{18}O_p$ in the sink region between the early Holocene and the LGM can be linearly decomposed into two components: changes in the intrinsic $\delta^{18}O_p$ composition of the sink region ($\Delta\delta^{18}O_{p,sin\,k,i} \times \frac{P_i}{P}$) and change associated with the precipitation weight ($\Delta\frac{P_i}{P} \times \delta^{18}O_{p,sin\,k,i}$), as shown in Equation (4a)[53]. Previous studies have suggested that precipitation weight changes reflect moisture source location change[52]. Where a variable is shown without the Δ notation, it denotes the climatological mean state. When summing over all source regions, changes in the intrinsic $\delta^{18}O_p$ composition are shown in Fig. 3b, while precipitation weight changes are shown in Fig. 3a.

$$\Delta\delta^{18}O_{p,sin\,k,i} = \Delta\delta^{18}O_{p,sin\,k,i} \times \frac{P_i}{P} + \Delta\frac{P_i}{P} \times \delta^{18}O_{p,sin\,k,i} \tag{4a}$$

The change in the intrinsic $\delta^{18}O_p$ composition in the sink region can be further decomposed into contributions from changes in vapor $\delta^{18}O$ ($\delta^{18}O_v$) composition at the tagged source regions, variations in upstream rainout or enroute depletion in $\delta^{18}O_v$, and shifts in the impact of local condensation enrichment on $\delta^{18}O_p$ in the sink regions, as detailed in Equation 4b[52]. The latter two processes are displayed in Supplementary Fig. 5a–b.

$$\begin{aligned} \Delta\delta^{18}O_{p,sink,i} \times \frac{P_i}{P} &= \Delta\delta^{18}O_{v,source,i} \times \frac{P_i}{P} \\ &+ \Delta\left(\delta^{18}O_{v,sink,i} - \delta^{18}O_{v,source,i}\right) \times \frac{P_i}{P} \\ &+ \Delta\left(\delta^{18}O_{p,sink,i} - \delta^{18}O_{v,sink,i}\right) \times \frac{P_i}{P} \end{aligned} \qquad (4b)$$

The term "local condensation changes" quantifies the shift in the isotopic difference between near-surface vapor $\delta^{18}O_v$ and $\delta^{18}O_p$ at the sink region. It integrates the net effect of multiple sub-cloud and condensation-zone processes that alter this difference, such as sub-cloud rain re-evaporation, shifts in condensation height, and local water vapor convergence[52,53]. An enrichment signature arises when processes like enhanced rain re-evaporation under drier conditions[55] or a lowered condensation level outweigh the depletion effect of in-cloud Rayleigh distillation[56].

Data availability

The data supporting this study are available as follows: (1) iTraCE and TRACE-21ka model simulation outputs are archived at the Earth System Grid Federation nodes https://gdex.ucar.edu/datasets/d651022/dataaccess/ and https://gdex.ucar.edu/datasets/d651050/dataaccess/; (2) Paleoclimate proxy data are publicly available from the NOAA (https://www.ncdc.noaa.gov/data-access/paleoclimatology-data); (3) The water-tagging experiments data used in this study are deposited in Zenodo at https://zenodo.org/records/18361391.

Code availability

The iCESM is freely available as open-source code from https://github.com/NCAR/iCESM1.2. Data analysis and plotting were performed with NCL (NCAR Command Language, version 6.6.2, https://www.ncl.ucar.edu/).

Reference

1. Wang, B. *et al.* Monsoons in Climate Change. *Bulletin of the American Meteorological Society*

103, 35–42 (2022).

2. Wang, P. X. *et al.* The global monsoon across timescales: Coherent variability of regional monsoons. *Clim. Past* **10**, 2007–2052 (2014).
3. An, Z. *et al.* Global monsoon dynamics and climate change. *Annu. Rev. Earth Planet. Sci.* **43**, 29–77 (2015).
4. Sun, Y., Clemens, S. C., An, Z. & Yu, Z. Astronomical timescale and palaeoclimatic implication of stacked 3.6-myr monsoon records from the Chinese loess plateau. *Quat. Sci. Rev.* **25**, 33–48 (2006).
5. Wang, Y. *et al.* Millennial- and orbital-scale changes in the east Asian monsoon over the past 224,000 years. *Nature* **451**, 1090–1093 (2008).
6. Cheng, H. *et al.* Chinese stalagmite paleoclimate researches: A review and perspective. *Sci. China Earth Sci.* **62**, 1489–1513 (2019).
7. Cheng, H. *et al.* Orbital-scale Asian summer monsoon variations: Paradox and exploration. *Sci. China Earth Sci.* **64**, 529–544 (2021).
8. Maher, B. A. Holocene variability of the east Asian summer monsoon from Chinese cave records: A re-assessment. *Holocene* **18**, 861–866 (2008).
9. Sun, Y. *et al.* Astronomical and glacial forcing of east Asian summer monsoon variability. *Quat. Sci. Rev.* **115**, 132–142 (2015).
10. Beck, J. W. *et al.* A 550,000-year record of east Asian monsoon rainfall from 10Be in loess. *Science* **360**, 877–881 (2018).
11. Cheng, H. *et al.* The Asian monsoon over the past 640,000 years and ice age terminations. *Nature* **534**, 640–646 (2016).
12. Cai, Y. *et al.* Variability of stalagmite-inferred Indian monsoon precipitation over the past

252,000 y. *Proc. Natl. Acad. Sci. U. S. A.* **112**, 2954–2959 (2015).

13. Liu, G. *et al.* On the glacial-interglacial variability of the Asian monsoon in speleothem δ^{18}O records. *Sci. Adv.* **6**, eaay8189 (2020).
14. Zhang, Z. *et al.* Summer and nonsummer climatic signals in speleothem δ^{18}O revealed by loess microcodium δ^{18}O in east Asia. *Proc. Natl. Acad. Sci. U.S.A.* **122**, e2425565122 (2025).
15. Pausata, F. S. R., Battisti, D. S., Nisancioglu, K. H. & Bitz, C. M. Chinese stalagmite δ^{18}O controlled by changes in the Indian monsoon during a simulated heinrich event. *Nat. Geosci.* **4**, 474–480 (2011).
16. Liu, Z. *et al.* Chinese cave records and the east Asia summer monsoon. *Quat. Sci. Rev.* **83**, 115–128 (2014).
17. Hu, J., Emile-Geay, J., Tabor, C., Nusbaumer, J. & Partin, J. Deciphering oxygen isotope records from Chinese speleothems with an isotope-enabled climate model. *Paleoceanogr. Paleoclimatol.* **34**, 2098–2112 (2019).
18. He, C. *et al.* Hydroclimate footprint of pan-Asian monsoon water isotope during the last deglaciation. *Sci. Adv.* **7**, eabe2611 (2021).
19. Jing, Z. *et al.* Precipitation oxygen isotope variability across timescales in East Asia records two sub-processes of summer monsoon system. *Commun Earth Environ* **6**, 513 (2025).
20. Zhang, J. *et al.* Upstream moisture sources and circulation patterns controls Asian monsoon hydroclimate over the past 20,000 years. *Quat. Sci. Rev.* **363**, 109438 (2025).
21. Liu, X., Xie, X., Guo, Z., Yin, Z.-Y. & Chen, G. Model-based orbital-scale precipitation δ^{18}O variations and distinct mechanisms in Asian monsoon and arid regions. *Natl. Sci. Rev.* **9**, nwac182 (2022).
22. Wen, Q. *et al.* Grand dipole response of Asian summer monsoon to orbital forcing. *npj Clim.*

Atmos. Sci. **7**, 1–11 (2024).

23. Dutt, S. *et al.* Abrupt changes in Indian summer monsoon strength during 33,800 to 5500 years B.P. *Geophys. Res. Lett.* **42**, 5526–5532 (2015).
24. Wang, Y. J. *et al.* A high-resolution absolute-dated late pleistocene monsoon record from Hulu cave, China. *Science* **294**, 2345–2348 (2001).
25. Wu, J., Wang, Y., Cheng, H. & Edwards, L. R. An exceptionally strengthened East Asian summer monsoon event between 19.9 and 17.1 ka BP recorded in a Hulu stalagmite. *Sci. China Ser. D-Earth Sci.* **52**, 360–368 (2009).
26. Zhang, H. *et al.* East Asian hydroclimate modulated by the position of the westerlies during termination I. *Science* **362**, 580–583 (2018).
27. Wang, Z. *et al.* A high-resolution stalagmite record from Luoshui Cave, Central China over the past 23.5 kyr. *Quat. Sci. Rev.* **282**, 107443 (2022).
28. Li, T.-Y. *et al.* High precise dating on the variation of the Asian summer monsoon since 37 ka BP. *Sci. Rep.* **11**, 9375 (2021).
29. Zhang, X. *et al.* Quantification of Asian monsoon variability from 68 ka BP through pollen-based climate reconstruction. *Sci. Bull.* **68**, 713–722 (2023).
30. Deplazes, G. *et al.* Links between tropical rainfall and north Atlantic climate during the last glacial period. *Nat. Geosci.* **6**, 213–217 (2013).
31. Sun, Y. *et al.* Influence of Atlantic meridional overturning circulation on the east Asian winter monsoon. *Nat. Geosci.* **5**, 46–49 (2012).
32. Chen, F. *et al.* East Asian summer monsoon precipitation variability since the last deglaciation. *Sci. Rep.* **5**, 11186 (2015).
33. Zheng, Z. *et al.* Holocene warming and evergreen/deciduous forest replacement across eastern

China. *Quat. Sci. Rev.* **307**, 108057 (2023).

34. He, C. *et al.* Enhanced or weakened western north pacific subtropical high under global warming? *Sci. Rep.* **5**, 16771 (2015).
35. Guo, Q.-Y. The summer monsoon intensity index in east Asia and its variation. *Acta Geogr. Sin.* **38**, 207–217 (1983).
36. Yim, S.-Y., Wang, B., Liu, J. & Wu, Z. A comparison of regional monsoon variability using monsoon indices. *Clim. Dyn.* **43**, 1423–1437 (2014).
37. Di Nezio, P. N. *et al.* The climate response of the Indo-Pacific warm pool to glacial sea level. *Paleoceanography* **31**, 866–894 (2016).
38. Huang, D., Liu, A., Zheng, Y. & Zhu, J. Inter-model spread of the simulated east Asian summer monsoon rainfall and the associated atmospheric circulations from the CMIP6 models. *J. Geophys. Res.: Atmos.* **127**, e2022JD037371 (2022).
39. Xue, D. *et al.* Robust projection of east Asian summer monsoon rainfall based on dynamical modes of variability. *Nat. Commun.* **14**, 3856 (2023).
40. Dayem, K. E., Molnar, P., Battisti, D. S. & Roe, G. H. Lessons learned from oxygen isotopes in modern precipitation applied to interpretation of speleothem records of paleoclimate from eastern Asia. *Earth and Planetary Science Letters* **295**, 219–230 (2010).
41. Zhang, H. *et al.* A data-model comparison pinpoints Holocene spatiotemporal pattern of east Asian summer monsoon. *Quat. Sci. Rev.* **261**, 106911 (2021).
42. Wang, M. *et al.* Stalagmite records of spatiotemporal hydroclimatic variations in monsoonal China during 47–12 ka BP. *Global Planet. Change* **244**, 104639 (2025).
43. Yun, K.-S. *et al.* Increasing ENSO–rainfall variability due to changes in future tropical temperature–rainfall relationship. *Commun. Earth Environ.* **2**, 43 (2021).

44. Brady, E. *et al.* The connected isotopic water cycle in the community earth system model version 1. *JAMES* **11**, 2547–2566 (2019).

45. Hurrell, J. W. *et al.* The community earth system model: A framework for collaborative research. *Bull. Amer. Meteor. Soc.* **94**, 1339–1360 (2013).

46. Berger, A. Long-term variations of daily insolation and quaternary climatic changes. *Journal of the Atmospheric Sciences* **35**, 2362 (1978).

47. Lüthi, D. *et al.* High-resolution carbon dioxide concentration record 650,000–800,000 years before present. *Nature* **453**, 379–382 (2008).

48. Liu, Z. *et al.* Transient simulation of last deglaciation with a new mechanism for Bølling-Allerød warming. *Science* **325**, 310–314 (2009).

49. Nusbaumer, J., Wong, T. E., Bardeen, C. & Noone, D. Evaluating hydrological processes in the community atmosphere model version 5 (CAM5) using stable isotope ratios of water. *JAMES* **9**, 949–977 (2017).

50. Coplen, T. B., Kendall, C. & Hopple, J. Comparison of stable isotope reference samples. *Nature* **302**, 236–238 (1983).

51. O'Neil, J. R., Clayton, R. N. & Mayeda, T. K. Oxygen isotope fractionation in divalent metal carbonates. *J. Chem. Phys.* **51**, 5547–5558 (1969).

52. Bao, Y., Liu, Z. & He, C. Dipole response of millennial variability in tropical south American precipitation and $\delta^{18}O_p$ during the last deglaciation. Part II: $\delta^{18}O_p$ response. *J. Clim.* **36**, 4709–4721 (2023).

53. Tabor, C. R. *et al.* Interpreting precession-driven $\delta^{18}O$ variability in the south Asian monsoon region. *J. Geophys. Res.: Atmos.* **123**, 5927–5946 (2018).

54. Draxler, R. R. & Hess, G. D. An overview of the HYSPLIT_4 modelling system for trajectories.

Aust. Meteorol. Mag. **47**, (1998).

55. Worden, J., Noone, D. & Bowman, K. Importance of rain evaporation and continental convection in the tropical water cycle. *Nature* **445**, 528–532 (2007).
56. Risi, C. *et al.* Understanding the Sahelian water budget through the isotopic composition of water vapor and precipitation. *J. Geophys. Res.: Atmos.* **115**, (2010).

Figure Captions

Fig. 1 | Pattern and time series of $\delta^{18}O_c$ and $\delta^{18}O_p$ during the last deglaciation.

a Simulated $\delta^{18}O_p$ difference pattern between the early Holocene (11.5–11 ka) and the LGM (20–19.5 ka). Shaded areas denote differences that are robust against internal variability ($p < 0.05$, two-tailed Student's *t*-test). Speleothem $\delta^{18}O_c$ sample locations are marked by points, with colors corresponding to anomaly alignment with the modeled difference pattern. The purple box outlines the study area in South Asia and eastern China. **b** Anomaly time series for South Asia records, relative to the last deglaciation mean. Records include southeastern Yunnan caves (SEY, pink)[13], eastern coastal Bay of Bengal caves (CBOB, yellow)[13], Mawmluh Cave (Maw, purple)[23], and Xiaobailong Cave (XBL, blue)[12]. **c** Anomaly time series for eastern China records, relative to the last deglaciation mean. Records include Furong Cave (FR, pink)[28], Luoshui Cave (LS, yellow)[27], Haozhu Cave (HZ, purple)[26], and Hulu Cave (HL, blue)[24,25]. The black line is the multi-record ensemble mean of $\delta^{18}O_c$. The grey line is the modeled $\delta^{18}O_c$ from the full-forcing simulation, calculated as the ensemble mean at the record locations. Values in the legend are $\delta^{18}O_c$ anomalies between 11 and 20 ka.

Fig. 2 | Patterns of precipitation and monsoon circulation changes between the early Holocene and the LGM.

a Summer precipitation climatology (shading, mm day^{-1}) and 850-hPa winds (vector, m s^{-1}) at the

LGM. **b** Same as (**a**) but for the difference between 11 and 20 ka. Speleothem $\delta^{18}O_c$ sample locations (from Fig. 1a) are overlaid as dots. **c** Summer surface temperature anomalies (shading, °C), with the boundaries of the western Pacific Subtropical High (WPSH), defined by the zero value of 500-hPa eddy geopotential height, shown for 11 ka (green contour) and 20 ka (blue contour). The eddy geopotential height is calculated as the geopotential height minus the area-averaged height over 0–40°N, 0–360°E[34]. **d** 500-hPa vertical velocity anomalies (Pa s^{-1}), where positive (negative) values denote downward (upward) motion. Shaded areas denote differences that are robust against internal variability ($p < 0.05$, two-tailed Student's *t*-test).

Fig. 3 | Decomposition of annual $\delta^{18}O_p$ response between the early Holocene and the LGM.

a Contribution from changes in precipitation weighting ($\Delta\frac{P_i}{P} \times \delta^{18}O_{p,i}$). **b** Contribution from changes in the intrinsic isotopic value ($\Delta\delta^{18}O_{p,i} \times \frac{P_i}{P}$). The sum of (**a**) and (**b**) equals the total $\delta^{18}O_p$ change (see Equation 3). The purple box outlines South Asia and eastern China. **c**, **e** Contributions of the Pacific and Indian Ocean source regions, respectively, to the term shown in (**a**). **d**, **f** Contributions of the same source regions to the term shown in (**b**).

Fig. 4 | Changes in $\delta^{18}O_p$ patterns between the early Holocene and the LGM under different external forcings.

a–d Spatial patterns of $\delta^{18}O_p$ difference in response to (**a**) All-forcing (ICE+ORB+GHG+MWF), (**b**) ICE, (**c**) ORB, and (**d**) GHG forcing. The MWF is not displayed separately as its net difference between these two periods is negligible. Shaded areas denote differences that are robust against internal variability ($p < 0.05$, two-tailed Student's *t*-test). **e** Boxplots of regional mean $\delta^{18}O_p$ responses over South Asia (green) and eastern China (brown) to All, ICE, ORB, and GHG forcings. In each boxplot, horizontal lines indicate means, box edges represent ±1 standard deviation, and whiskers show the "very likely" range (5–95%). Numerical labels denote regional $\delta^{18}O_p$

differences (South Asia minus eastern China) under each forcing: All (1.54‰), ICE (0.83‰), ORB (0.24‰), and GHG (0.46‰).

Fig. 5 | Patterns of atmospheric circulation changes between the early Holocene and the LGM under different external forcings.

Panels **a** and **b** show the response to ICE forcing: (**a**) summer surface temperature anomalies (shading, °C) and (**b**) precipitation anomalies (shading, mm day^{-1}) and 850-hPa wind (vector, m s^{-1}) anomalies. Green and blue lines in (**a**) indicate the western Pacific Subtropical High (WPSH) positions at 11 and 20 ka, respectively. **c**, **d**, Same as (**a**, **b**) but for the response to ORB forcing. **e**, **f**, Same as (**a**, **b**) but for the response to GHG forcing. Shaded areas denote differences that are robust against internal variability ($p < 0.05$, two-tailed Student's *t*-test).

Fig. 6 | Schematic diagram for the response of $\delta^{18}O_p$ between the early Holocene and the LGM.

The green (brown) shading indicates the depleted (enriched) $\delta^{18}O_p$. The blue arrows mark the main moisture sources in forming the $\delta^{18}O_p$ change over the East Asia, with solid (dashed) arrows indicating that the pathway is strengthened (weakened). The red arrow represents enhanced evaporation.

Acknowledgments

We thank the reconstruction and modeling teams for providing the proxy data and iTRACE/TRACE simulations. Our study was supported by the National Natural Science Foundation of China (Grant No. 42130604), the National Key Research and Development Program of China (Grant No. 2023YFF0804704), and the Priority Academic Program Development of Jiangsu Higher Education Institutions (Grant No. 164320H116).

Author contributions

X. W., W. S. conceptualized and led the work. X. W., W. S. ran the experiments and wrote the initial draft. J. L., Y. B., L. N., Q. W., J. H., and Y. M. contributed to data analysis including validation and interpretation of the results. K. Z., Y. W., and K. C. provided the reconstruction data and clues for data interpretation. All authors reviewed and edited the manuscript.

Competing interests

The authors declare no competing interests.

Editorial summary:

A weak glacial-interglacial isotopic signal in eastern China reflects compensatory processes in atmospheric moisture routing and local recycling, primarily orchestrated by ice-sheet forcing, according to speleothem records,
climate simulations, and water-tagging experiments.

Peer review information:

Communications Earth and Environment thanks the anonymous reviewers for their contribution to the peer review of this work. Primary Handling Editors: Kyung-Sook Yun and Nicola Colombo. [A peer review file is available.]

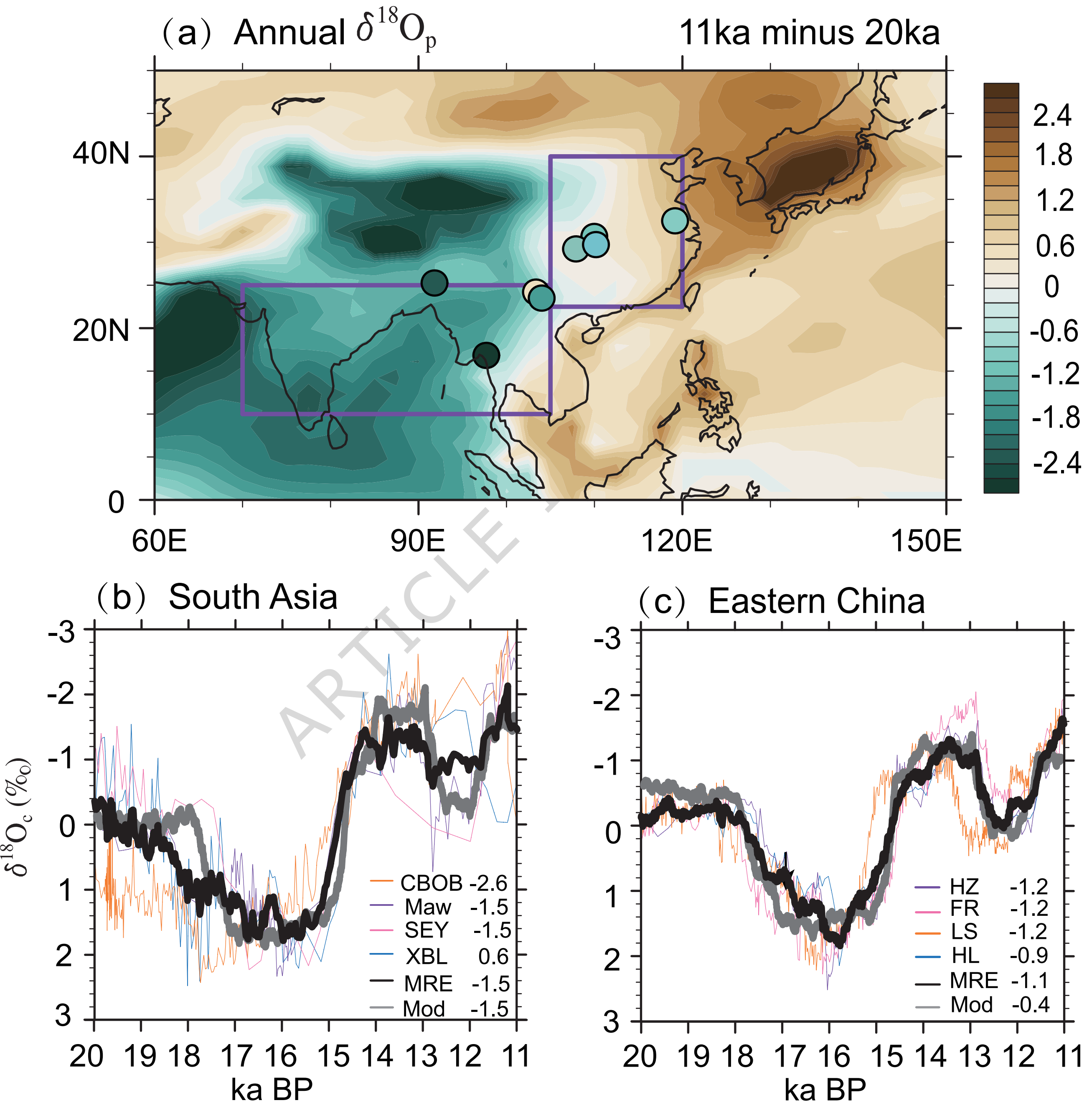
(a) Annual $\delta^{18}O_p$
11ka minus 20ka
40N
20N
0
60E
90E
120E
150E
2.4
1.8
1.2
0.6
0
-0.6
-1.2
-1.8
-2.4
(b) South Asia
$\delta^{18}O_c$ (‰)
-3
-2
-1
0
1
2
3
20 19 18 17 16 15 14 13 12 11
ka BP
CBOB -2.6
Maw -1.5
SEY -1.5
XBL 0.6
MRE -1.5
Mod -1.5
(c) Eastern China
-3
-2
-1
0
1
2
3
20 19 18 17 16 15 14 13 12 11
ka BP
HZ -1.2
FR -1.2
LS -1.2
HL -0.9
MRE -1.1
Mod -0.4

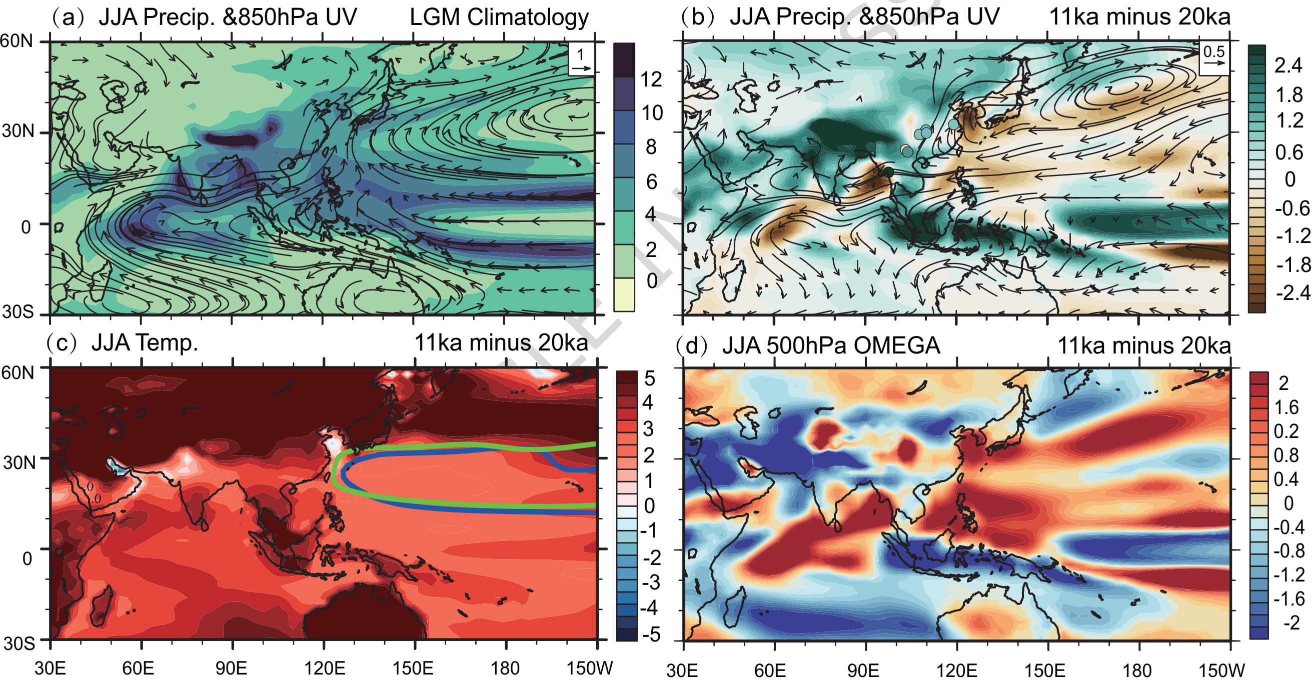
(a) JJA Precip. &850hPa UV
LGM Climatology
(b) JJA Precip. &850hPa UV
11ka minus 20ka
(c) JJA Temp.
11ka minus 20ka
(d) JJA 500hPa OMEGA
11ka minus 20ka
1
0.5
60N
30N
0
30S
30E
60E
90E
120E
150E
180
150W
12
10
8
6
4
2
0
2.4
1.8
1.2
0.6
0
-0.6
-1.2
-1.8
-2.4
5
4
3
2
1
0
-1
-2
-3
-4
-5
2
1.6
0.2
0.8
0.4
0
-0.4
-0.8
-1.2
-1.6
-2

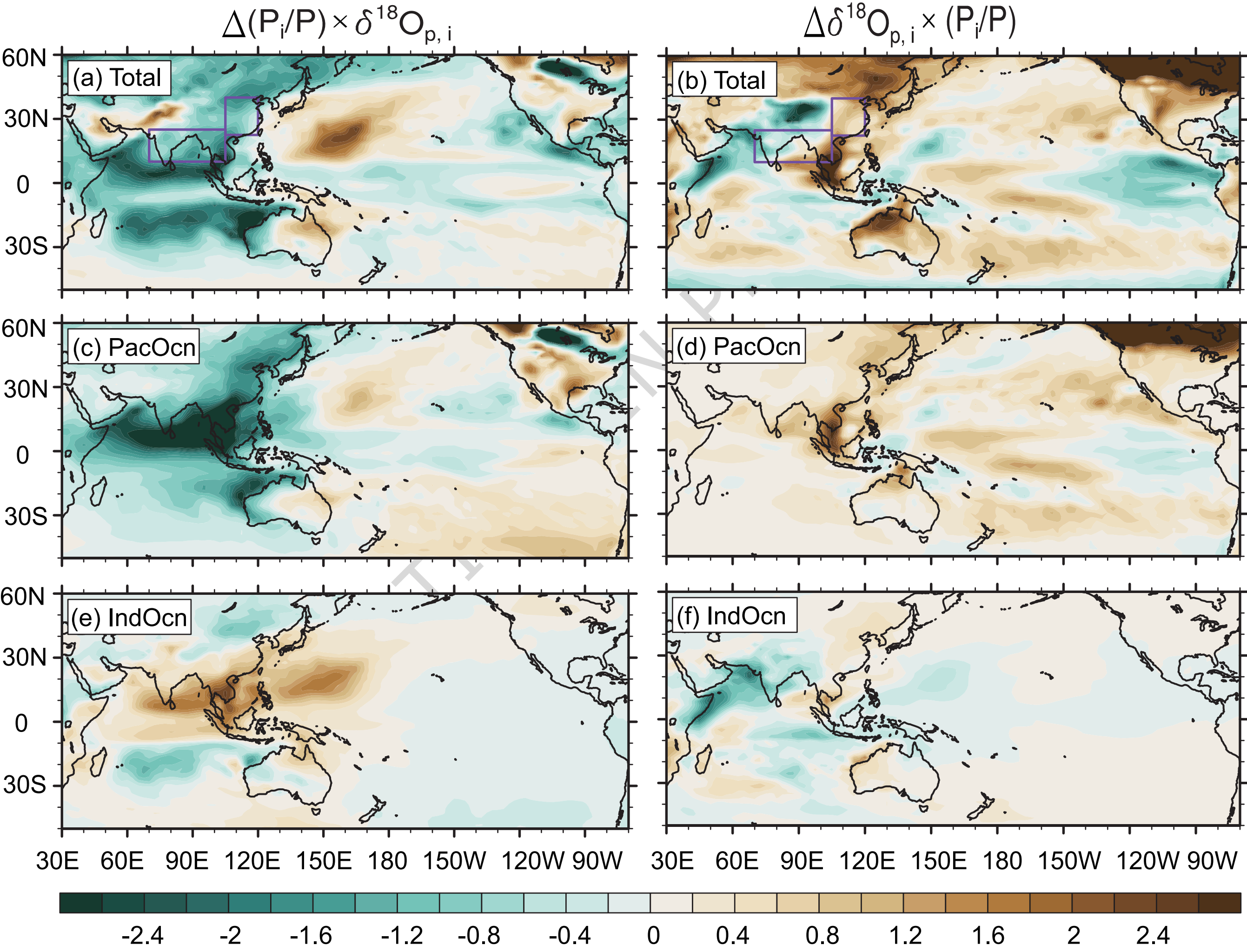
$\Delta(P_i/P) \times \delta^{18}O_{p,i}$
$\Delta\delta^{18}O_{p,i} \times (P_i/P)$
(a) Total
(b) Total
(c) PacOcn
(d) PacOcn
(e) IndOcn
(f) IndOcn
60N
30N
0
30S
30E
60E
90E
120E
150E
180
150W
120W
90W
-2.4
-2
-1.6
-1.2
-0.8
-0.4
0
0.4
0.8
1.2
1.6
2
2.4

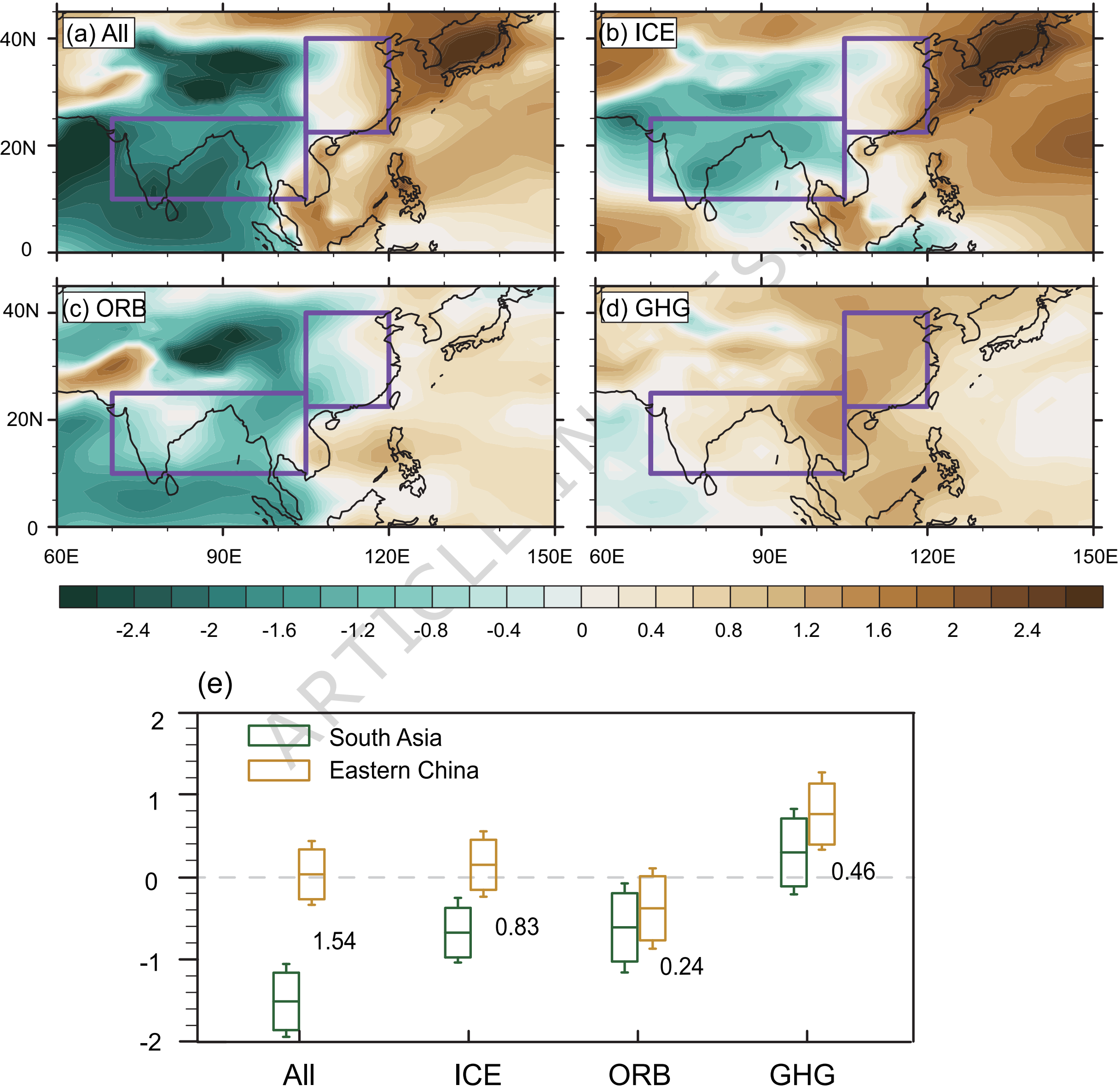
(a) All
(b) ICE
(c) ORB
(d) GHG
40N
20N
0
60E
90E
120E
150E
-2.4
-2
-1.6
-1.2
-0.8
-0.4
0
0.4
0.8
1.2
1.6
2
2.4
(e)
South Asia
Eastern China
2
1
0
-1
-2
1.54
0.83
0.24
0.46
All
ICE
ORB
GHG

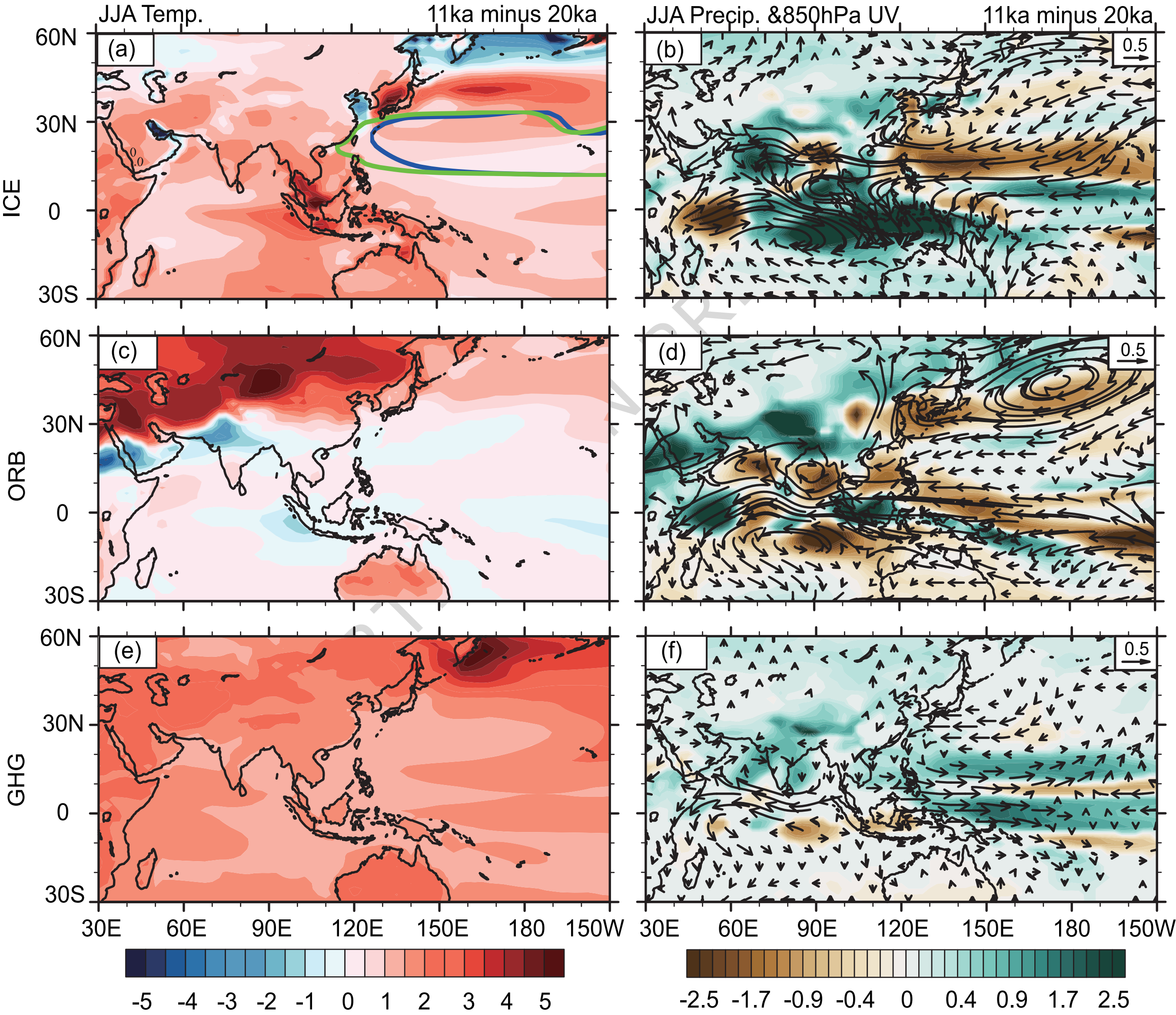
JJA Temp.
11ka minus 20ka
JJA Precip. &850hPa UV
11ka minus 20ka
(a)
(b)
(c)
(d)
(e)
(f)
ICE
ORB
GHG
0.5
60N
30N
0
30S
30E
60E
90E
120E
150E
180
150W
-5
-4
-3
-2
-1
0
1
2
3
4
5
-2.5
-1.7
-0.9
-0.4
0
0.4
0.9
1.7
2.5

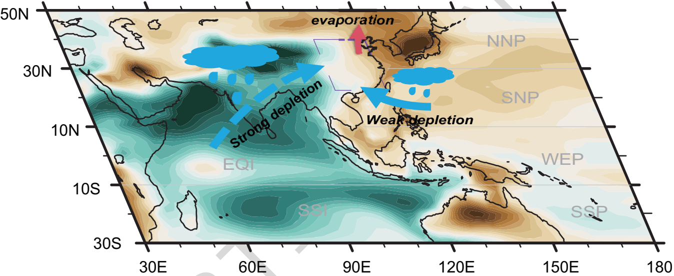
evaporation
NNP
SNP
Strong depletion
Weak depletion
WEP
EQI
SSI
SSP
50N
30N
10N
10S
30S
30E
60E
90E
120E
150E
180